

Optimization of the absorption efficiency of an amorphous-silicon thin-film tandem solar cell backed by a metallic surface-relief grating

Manuel Solano,¹ Muhammad Faryad,² Anthony S. Hall,³ Thomas E. Mallouk,³ Peter B. Monk,¹ and Akhlesh Lakhtakia^{2,*}

¹Department of Mathematical Sciences, University of Delaware, Newark, Delaware 19716, USA

²Nanoengineered Metamaterials Group, Department of Engineering Science and Mechanics, Pennsylvania State University, University Park, Pennsylvania 16802, USA

³Department of Chemistry, Pennsylvania State University, University Park, Pennsylvania 16802, USA

*Corresponding author: akhlesh@psu.edu

Received 5 September 2012; revised 5 December 2012; accepted 30 December 2012; posted 2 January 2013 (Doc. ID 175451); published 7 February 2013

The rigorous coupled-wave approach was used to compute the plane-wave absorptance of a thin-film tandem solar cell with a metallic surface-relief grating as its back reflector. The absorptance is a function of the angle of incidence and the polarization state of incident light; the free-space wavelength; and the period, duty cycle, the corrugation height, and the shape of the unit cell of the surface-relief grating. The solar cell was assumed to be made of hydrogenated amorphous-silicon alloys and the back reflector of bulk aluminum. The incidence and the grating planes were taken to be identical. The AM1.5 solar irradiance spectrum was used for computations in the 400–1100 nm wavelength range. Inspection of parametric plots of the solar-spectrum-integrated (SSI) absorption efficiency and numerical optimization using the differential evolution algorithm were employed to determine the optimal surface-relief grating. For direct insolation, the SSI absorption efficiency is maximizable by appropriate choices of the period, the duty cycle, and the corrugation height, regardless of the shape of the corrugation in each unit cell of the grating. A similar conclusion also holds for diffuse insolation, but the maximum efficiency for diffuse insolation is about 20% smaller than for direct insolation. Although a tin-doped indium-oxide layer at the front and an aluminum-doped zinc-oxide layer between the semiconductor material and the backing metallic layer change the optimal depth of the periodic corrugations, the optimal period of the corrugations does not significantly change. © 2013 Optical Society of America

OCIS codes: 230.1950, 250.5403, 260.1960, 350.6050.

1. Introduction

For the last three decades, research to bring down the cost of photovoltaic (PV) solar cells has gained huge momentum, and many strategies to increase the efficiency of light harvesting by solar cells have been investigated. Among these strategies [1] is the use of plasmonic structures to enhance the absorption of light by PV solar cells [2–4]. In this context,

a basic idea is to periodically texture the metallic back reflector of a thin-film solar cell on the sub-wavelength scale. Whereas the use of a metallic surface-relief grating as a back reflector has been investigated for at least three decades to enhance the optical absorptance of solar cells [5,6], only recently has this enhancement been interpreted in terms of the excitation of surface-plasmon-polariton (SPP) waves guided by the semiconductor/metal interface [4].

Thin-film solar cells containing amorphous-silicon alloys offer a possible route to produce energy on a

1559-128X/13/050966-14\$15.00/0
© 2013 Optical Society of America

large scale more cheaply than crystalline-silicon solar cells [7]. Amorphous silicon is well suited for this task because a layer that is only a few hundred nanometers in thickness is required to effectively absorb a large fraction of visible light incident on it [8]. However, amorphous silicon absorbs light in the near-infrared (NIR) regime poorly, because a thickness of several tens of micrometers is needed [8]. But the NIR portion of the AM1.5 solar radiation is very significant. Although incomplete absorption of the NIR portion is a major contributor to the low efficiency of thin-film amorphous-silicon solar cells, the thickness of the amorphous-silicon layer cannot be enhanced without sacrificing desirable electrical characteristics [8].

An alternative to increasing the thickness of the amorphous-silicon layer is the periodic subwavelength-texturing of the metallic back reflector [5,6,9–12]. The consequent enhancement in the efficiency depends on the shape and dimensions of the unit cell of the metallic surface-relief grating that forms the back reflector [13]. However, optimization is done after an inspection of the results from a chosen set of surfaces, but optimization algorithms have not been pressed into service.

In this paper, we present theoretical investigations on the optimization of absorption of light by an amorphous-silicon tandem solar cell by finding an optimal metallic surface-relief grating. We assume that the active part of the solar cell comprises several semiconductor layers, whose thicknesses are fixed at (electrically) optimal values, but that the geometric parameters of the unit cell of the surface-relief grating and the angle of incidence are taken as free parameters. The boundary-value problem modeling this solar cell is presented in Section 2 and solved using the rigorous coupled-wave approach (RCWA) [14,15], which has been used in several studies of nanostructured amorphous-silicon solar cells [12,16,17]. The RCWA solves the frequency-domain Maxwell equations directly and, therefore, takes into account all possible electromagnetic wave phenomena, including waveguide modes, localized SPP resonances, and SPP waves. The key feature of the RCWA is the representation of the relative permittivity as a Fourier series and the field phasors in terms of Floquet harmonics. The accuracy of the RCWA solution depends upon the number of terms used in the expansions of the relative permittivity and field phasors.

The optimization was carried out in two ways: (i) direct inspection of parametric plots obtained from RCWA calculations and (ii) the differential evolution algorithm (DEA) [18–20] described in Section 3. Numerical results for the optimization of the free parameters for three types of metallic surface-relief gratings are discussed in Section 4 for both direct insolation and diffuse insolation. The effects of the inclusion of two transparent-conducting-oxide layers—an aluminum-doped zinc oxide (AZO) layer between the metallic surface-relief grating and the deepest semiconducting layer, and a tin-doped

indium-oxide (commonly abbreviated as ITO) layer as the front layer—are also studied in Section 4. Concluding remarks are presented in Section 5.

An $\exp(-i\omega t)$ time-dependence is implicit, with ω denoting the angular frequency. The free-space wave-number and the free-space wavelength are denoted by $k_0 = \omega/\sqrt{\epsilon_0\mu_0}$ and $\lambda_0 = 2\pi/k_0$, respectively, with μ_0 and ϵ_0 being the permeability and permittivity of free space. Vectors are in boldface, and the Cartesian unit vectors are denoted by $\hat{\mathbf{u}}_x$, $\hat{\mathbf{u}}_y$, and $\hat{\mathbf{u}}_z$.

2. Boundary-Value Problem

Let us now consider the boundary-value problem shown schematically in Fig. 1. The regions $z < 0$ and $z > L_t = L_d + L_g + L_m$ are vacuous. The region $0 \leq z \leq L_d$ is occupied by a multilayered material with its relative permittivity $\epsilon_d(z)$ being a piecewise constant function of z and $\text{Re}[\epsilon_d(z)] > 0$.

The region $L_d + L_g \leq z \leq L_t$ is occupied by a metal of relative permittivity ϵ_m , $\text{Re}(\epsilon_m) < 0$. The region $L_d < z < L_d + L_g$ contains a periodically undulating surface of period L along the x axis and corrugation height L_g . With $0 < L_g < d_a$ (see Fig. 1), the relative permittivity

$$\epsilon_g(x, z) = \epsilon_g(x \pm L, z) = \begin{cases} \epsilon_d(z), & z < g(x), \\ \epsilon_m, & z > g(x), \end{cases} \quad (1)$$

for $x \in (0, L)$ and $z \in (L_d, L_d + L_g)$, where the grating function $g(x)$ can be chosen to represent a desired shape for the unit cell of the surface-relief grating.

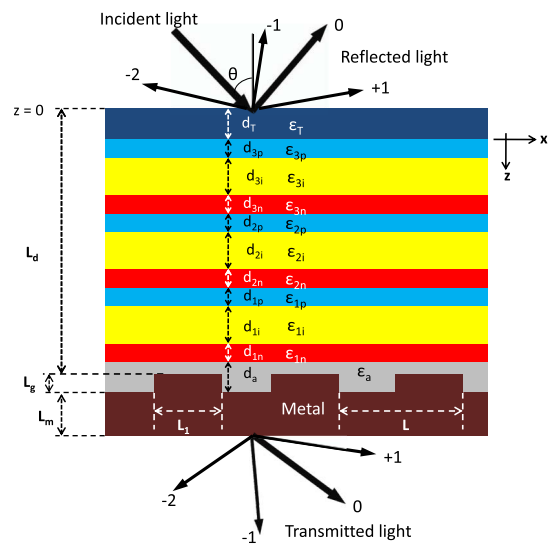


Fig. 1. (Color online) Schematic of the tandem solar cell with a metallic surface-relief grating as the back reflector. The ITO layer is dark blue, the intrinsic semiconductor layers are yellow, the p-type semiconductor layers are blue, the n-type semiconductor layers are red, and the layer in contact with the metal is gray. Specular components of the reflected and transmitted light are identified as of order 0, whereas nonspecular components are identified as of nonzero orders. The function $g(x)$ was chosen so that the fraction $\zeta = L_1/L$ of each unit cell is a corrugation and sunken while the fraction $1 - \zeta$ is flat.

Figure 1 contains 11 layers, of which the layer in contact with the metal surface-relief grating has a relative permittivity ϵ_a . This layer may either be made of an n-type semiconductor (Sections 4.A and 4.B) or AZO (Section 4.C). A tandem of three triplets of layers follows, each triplet being a p-i-n cell comprising a layer of an n-type semiconductor, a layer of an intrinsic semiconductor, and a layer of a p-type semiconductor. Absorption of light for conversion to electricity occurs only in the intrinsic semiconductor layers when the solar cell is made of amorphous silicon, for which reason these layers are also called *absorber layers*. Thus, the optimization problem tackled is that of a tandem solar cell backed by a metallic reflector with a periodically undulating surface. Our formulation in this section is general enough to accommodate fewer or more triplets [21]. Finally, the eleventh layer ($0 \leq z \leq d_T$) in the sequence is made of ITO (Section 4.C).

In the vacuous half-space $z \leq 0$, let a plane wave propagating in the xz plane at an angle θ with respect to the z axis be incident on the structure. Hence, the incident, reflected, and transmitted electric field phasors may be written in terms of Floquet harmonics as [22]:

$$\mathbf{E}_{\text{inc}}(\mathbf{r}) = \sum_{n \in \mathbb{Z}} (\hat{\mathbf{u}}_y a_s^{(n)} + \mathbf{p}_n^+ a_p^{(n)}) \times \exp[i(k_x^{(n)} x + k_z^{(n)} z)], \quad z \leq 0, \quad (2)$$

$$\mathbf{E}_{\text{ref}}(\mathbf{r}) = \sum_{n \in \mathbb{Z}} (\hat{\mathbf{u}}_y r_s^{(n)} + \mathbf{p}_n^- r_p^{(n)}) \times \exp[i(k_x^{(n)} x - k_z^{(n)} z)], \quad z \leq 0, \quad (3)$$

$$\mathbf{E}_{\text{tr}}(\mathbf{r}) = \sum_{n \in \mathbb{Z}} (\hat{\mathbf{u}}_y t_s^{(n)} + \mathbf{p}_n^+ t t_p^{(n)}) \times \exp\{i[k_x^{(n)} x + k_z^{(n)}(z - L_t)]\}, \quad z \geq L_t, \quad (4)$$

where $\mathbb{Z} = \{0, \pm 1, \pm 2, \dots\}$, $k_x^n = k_0 \sin \theta + n\kappa_x$, $\kappa_x = 2\pi/L$,

$$k_z^{(n)} = \begin{cases} +\sqrt{k_0^2 - (k_x^{(n)})^2}, & k_0^2 > (k_x^{(n)})^2 \\ +i\sqrt{(k_x^{(n)})^2 - k_0^2}, & k_0^2 < (k_x^{(n)})^2 \end{cases} \quad (5)$$

and

$$\mathbf{p}_n^\pm = \mp \frac{k_z^{(n)}}{k_0} \hat{\mathbf{u}}_x + \frac{k_x^{(n)}}{k_0} \hat{\mathbf{u}}_z. \quad (6)$$

The subscripts p and s represent the p - and s -polarization states, respectively. Specular components of the reflected and transmitted light are of order $n = 0$ in Eqs. (2)–(4), whereas nonspecular components are of orders $n \neq 0$.

The incidence amplitudes $\{a_p^{(n)}, a_s^{(n)}\}_{n \in \mathbb{Z}}$ are presumed known. For plane-wave incidence, $a_p^{(n)} = a_s^{(n)} = 0 \forall n \neq 0$; furthermore, $a_p^{(0)} \neq 0$ and $a_s^{(0)} = 0$

for p -polarized incidence, and $a_p^{(0)} = 0$ and $a_s^{(0)} \neq 0$ for s -polarized incidence. The reflection amplitudes $\{r_p^{(n)}, r_s^{(n)}\}_{n \in \mathbb{Z}}$ and transmission amplitudes $\{t_p^{(n)}, t_s^{(n)}\}_{n \in \mathbb{Z}}$ have to be determined by solving a boundary-value problem.

That is done very conveniently by using the RCWA algorithm [22,23]. The relative permittivity in the region $0 \leq z \leq L_t$ is expanded as a Fourier series with respect to x , viz.,

$$\epsilon(x, z) = \sum_{n \in \mathbb{Z}} \epsilon^{(n)}(z) \exp(in\kappa_x x), \quad z \in [0, L_t], \quad (7)$$

where the z -dependent coefficients $\epsilon^{(n)}(z)$ are known. The electric and magnetic field phasors are similarly expanded in the same region as

$$\mathbf{E}(\mathbf{r}) = \sum_{n \in \mathbb{Z}} \mathbf{E}^{(n)}(z) \exp(ik_x^{(n)} x), \quad z \in [0, L_t] \quad (8)$$

and

$$\mathbf{H}(\mathbf{r}) = \sum_{n \in \mathbb{Z}} \mathbf{H}^{(n)}(z) \exp(ik_x^{(n)} x), \quad z \in [0, L_t]. \quad (9)$$

The expansions in Eqs. (8) and (9) can also be regarded as Floquet harmonics with unknown vector functions $\mathbf{E}^{(n)}(z)$ and $\mathbf{H}^{(n)}(z)$.

Since the right sides of Eqs. (2)–(4) and (7)–(9) contain infinite number of terms, RCWA requires restricting the index $n \in [-N_t, N_t]$. Details of the algorithm to solve for the unknown transmission and reflection amplitudes have been presented elsewhere [22].

As the plane of incidence and the plane of the surface-relief grating are identical, depolarization does not occur. For p -polarized incidence, we set all incidence coefficients except $a_p^{(0)}$ equal to zero and computed the modal reflectances

$$R_p^{(n)} = |r_p^{(n)}/a_p^{(0)}|^2 \text{Re}[k_z^{(n)}]/k_0 \cos \theta, \quad (10)$$

and modal transmittances

$$T_p^{(n)} = |t_p^{(n)}/a_p^{(0)}|^2 \text{Re}[k_z^{(n)}]/k_0 \cos \theta. \quad (11)$$

For s -polarized incidence, we set all incidence coefficients except $a_s^{(0)}$ equal to zero and computed the modal reflectances

$$R_s^{(n)} = |r_s^{(n)}/a_s^{(0)}|^2 \text{Re}[k_z^{(n)}]/k_0 \cos \theta, \quad (12)$$

and modal transmittances

$$T_s^{(n)} = |t_s^{(n)}/a_s^{(0)}|^2 \text{Re}[k_z^{(n)}]/k_0 \cos \theta. \quad (13)$$

Thus, the absorptance for p -polarized incident waves is given by

$$A_p = 1 - \sum_{n=-N_t}^{N_t} [R_p^{(n)} + T_p^{(n)}], \quad (14)$$

and for s-polarized incident waves is given by

$$A_s = 1 - \sum_{n=-N_t}^{N_t} [R_s^{(n)} + T_s^{(n)}]. \quad (15)$$

For computing all results presented in this paper, $N_t = 12$ was set, after ascertaining that this value is large enough to deliver absorptances converged to within 1%.

3. Differential Evolution Algorithm

We used the DEA [18,19] to seek an optimal design for the surface-relief grating backing the solar cell. The DEA often performs significantly better than genetic algorithms in exploring the space of candidate solutions [19,20]. Given an initial guess in this search space, the underlying strategy is to improve the candidate solution at every iteration step and does not require explicit gradients of the cost function. A large space of candidate solutions can be searched, but—since it is a metaheuristic algorithm—a global maximum is not guaranteed unless the search domain and the initial guess of the parameters to be optimized are chosen wisely. Therefore, we used this algorithm in conjunction with the conclusions gleaned from inspection of RCWA results. The basic features of the DEA are now explained briefly.

Let $\mathbf{v} = (v_1, v_2, v_3, \dots, v_n)$ denote a point in the search space for an optimization problem that can be varied to obtain an optimal design. We wish to find \mathbf{v}^{opt} that maximizes a cost function $C: S \subset \mathbb{R}^n \rightarrow \mathbb{R}$, where S is the search space and n is the number of components of \mathbf{v} . A crossover probability $C \in (0, 1)$, a differential weight $\alpha \in (0, 2)$, and a number M of random points have to be chosen beforehand.

The steps to find \mathbf{v}^{opt} are as follows:

- 1: Randomly initialize a set of M points in the search space:
 $\{\mathbf{v}^{(m)}\}_{m=1}^M \subset S$
- 2: **while** stopping criterion is not satisfied **do**
- 3: **for** each $\mathbf{v}^{(\nu)}$, $\nu \in \{1, M\}$, **do**
- 4: Randomly choose three different points $\mathbf{v}^{(m_1)}$, $\mathbf{v}^{(m_2)}$ and $\mathbf{v}^{(m_3)} \in \{\mathbf{v}^{(m)}\}_{m=1}^M$
- 5: Choose a random index $j \in \{1, \dots, n\}$
- 6: Define $\mathbf{w} = (w_1, w_2, w_3, \dots, w_n)$ as follows:
- 7: For all $\ell \in \{1, \dots, n\}$, let r_ℓ be a uniform random number between 0 and 1.
- 8: **if** $r_\ell < C$ or $\ell = j$ **then**
- 9: $w_m \leftarrow v_m^{(m_1)} + \alpha(v_m^{(m_2)} - v_m^{(m_3)})$
- 10: **else**
- 11: $w_m \leftarrow v_m^{(\nu)}$
- 12: **end if**
- 13: **if** $C(\mathbf{w}) > C(\mathbf{v}^{(\nu)})$ **then**
- 14: $\mathbf{v}^{(m)} \leftarrow \mathbf{w}$
- 15: **end if**
- 16: **end for**
- 17: Let \mathbf{v}^{opt} be the point such that $C(\mathbf{v}^{\text{opt}}) \geq C(\mathbf{v}^{(\nu)}) \forall \nu \in \{1, \dots, M\}$
- 18: **end while**

In our optimization work, we used $C = 0.7$, $\alpha = 0.8$, and $M = 20$ [24].

4. Numerical Results and Discussion

For the numerical results presented in this section, we set $L_m = 30$ nm, and aluminum was chosen as the metal. As the tandem solar cell is a multijunction spectrum-splitting cell [8,25], choices for the multilayered semiconductor material must be made carefully.

In order to minimize the parasitic absorption in the doped-semiconductor layers, we set $d_{1n} = d_{1p} = d_{2n} = d_{2p} = d_{3n} = d_{3p} = 10$ nm in Fig. 1. The thicknesses of all absorber layers were chosen to allow each of them to generate the same current, which is necessary since all individual p-i-n cells in a tandem solar cell must be current matched [8,25]: $d_{1i} = 190$ nm, $d_{2i} = 230$ nm, and $d_{3i} = 90$ nm. The various layers of the tandem solar cell are assumed to be made of hydrogenated amorphous-silicon alloys:

- a-SiC:H with band-gap $E_g = 1.94$ eV for all p-type layers,
- a-Si:H with band-gap $E_g = 1.8$ eV for all n-type layers,
- a-Si_{1-u}Ge_u:H with bandgap $E_g = 1.4$ eV for the intrinsic layer of thickness d_{1i} ,
- a-Si_{1-u}Ge_u:H with bandgap $E_g = 1.6$ eV for the intrinsic layer of thickness d_{2i} , and
- a-Si:H with bandgap $E_g = 1.69$ eV for the intrinsic layer of thickness d_{3i} .

The material with the widest bandgap was chosen for the topmost absorber layer in order to allow photons of higher energy to penetrate the next absorber layer, and so on [8]. Parenthetically, we note that the fixed semiconductor structure chosen may change with a change in the grating shape and with the inclusion of antireflection coatings, and more comprehensive optimization may be necessary.

The relative permittivities of the hydrogenated amorphous-silicon alloys and aluminum are plotted versus the free-space wavelength λ_0 in Figs. 2 and 3, respectively. The relative permittivities of the semiconductors were computed using a model provided by Ferlauto *et al.* [25], and the relative permittivity of bulk aluminum was computed from an approximate model provided by Rakić [26]. Let us note that hydrogenated amorphous-silicon alloys can be fabricated by plasma-enhanced chemical vapor deposition over planar as well as patterned templates [27]. The composition of the alloys can be controlled by the ratio of precursor gases (silane, hydrogen, methane, germane) and the deposition temperature [25].

To optimize the geometry of the surface-relief grating, attention was restricted to three types of corrugations—rectangular, sinusoidal, and trapezoidal—shown in Fig. 4. The corrugation-shape function $g(x)$ is defined as

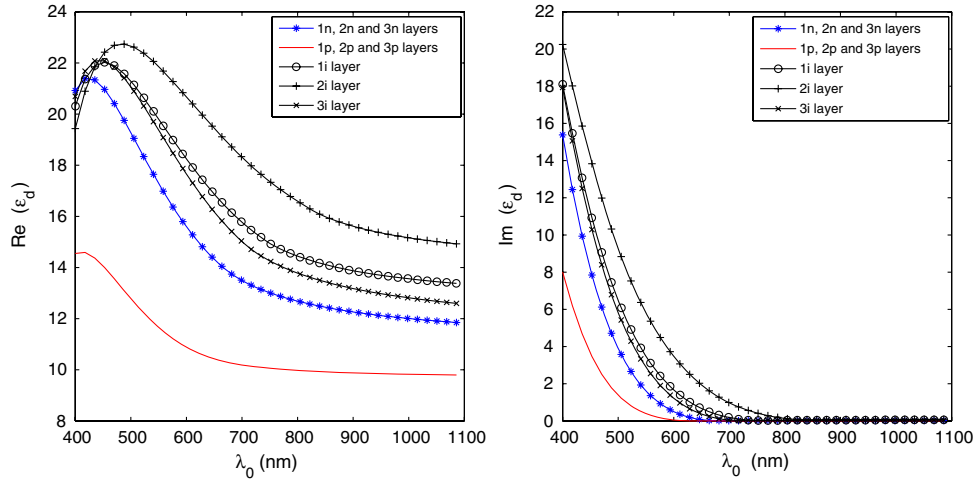


Fig. 2. (Color online) (Left) Real and (right) imaginary parts of the relative permittivities of all semiconductor layers as functions of the free-space wavelength. All p-type layers are made of a-SiC:H with bandgap $E_g = 1.94$ eV. All n-type layers are of a-Si:H with bandgap $E_g = 1.8$ eV. The top (1i) intrinsic layer is of a-Si_{1-u}Ge_u:H with bandgap $E_g = 1.4$ eV, the middle (2i) intrinsic layer is of a-Si_{1-u}Ge_u:H with bandgap $E_g = 1.6$ eV, and the bottom (3i) intrinsic layer is of a-Si:H with bandgap $E_g = 1.69$ eV.

$$g(x) = \begin{cases} L_d, & x \in (x_1, x_2) \\ L_d + L_g, & x \in (0, x_1) \cup (x_2, L) \end{cases} \quad (16)$$

for trapezoidal corrugations, where $x_1 = (L - L_1)/2$, $x_2 = (L + L_1)/2$, $x_3 = (L - L_2)/2$, and $x_4 = (L + L_2)/2$. Furthermore, $L_2 = L_1/2$ was taken for

for rectangular corrugations,

$$g(x) = \begin{cases} (L_d + L_g) - L_g \sin[\pi(x - x_1)/L_1], & x \in (x_1, x_2) \\ L_d + L_g, & x \in (0, x_1) \cup (x_2, L) \end{cases} \quad (17)$$

for sinusoidal corrugations, and

$$g(x) = \begin{cases} (L_d + L_g) - L_g(x - x_1)/(x_3 - x_1), & x \in (x_1, x_3) \\ L_d, & x \in (x_3, x_4) \\ (L_d + L_g) + L_g(x - x_2)/(x_2 - x_4), & x \in (x_4, x_2) \\ L_d + L_g, & x \in (0, x_1) \cup (x_2, L) \end{cases} \quad (18)$$

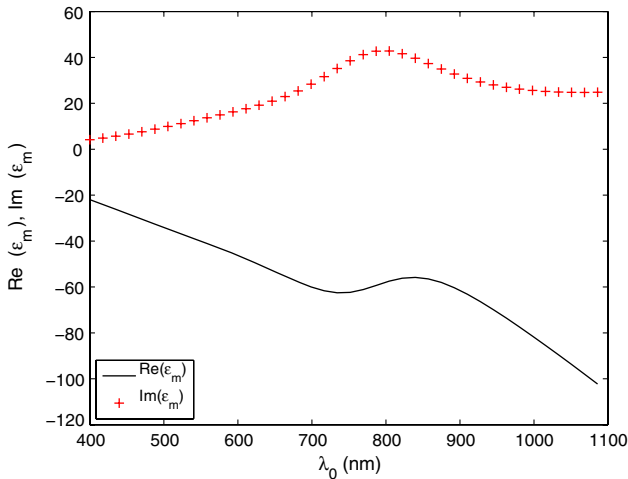


Fig. 3. (Color online) Real and imaginary parts of the relative permittivity of bulk aluminum as functions of the free-space wavelength.

the trapezoidal corrugations. The ratio $\zeta = L_1/L$ is called the duty cycle.

For optimization, the solar-spectrum-integrated (SSI) absorption efficiency was defined by

$$\eta_p(L, \zeta, L_g, \theta) := \frac{\int_{\lambda_{\min}}^{\lambda_{\max}} A_p(\lambda_0, L, \zeta, L_g, \theta) \lambda_0 S(\lambda_0) d\lambda_0}{\int_{\lambda_{\min}}^{\lambda_{\max}} \lambda_0 S(\lambda_0) d\lambda_0} \quad (19)$$

for p-polarized incidence, and by

$$\eta_s(L, \zeta, L_g, \theta) := \frac{\int_{\lambda_{\min}}^{\lambda_{\max}} A_s(\lambda_0, L, \zeta, L_g, \theta) \lambda_0 S(\lambda_0) d\lambda_0}{\int_{\lambda_{\min}}^{\lambda_{\max}} \lambda_0 S(\lambda_0) d\lambda_0} \quad (20)$$

for s-polarized incidence, and we chose

$$\eta := (\eta_p + \eta_s)/2 \quad (21)$$

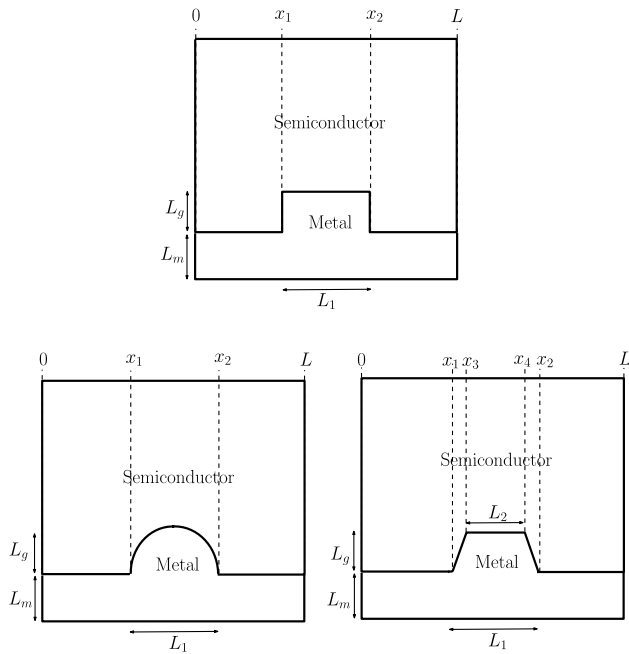


Fig. 4. Unit cell of a surface-relief grating with a (top) rectangular corrugation, (bottom left) sinusoidal corrugation, or (bottom right) trapezoidal corrugation, used for optimization.

for unpolarized light coming from the Sun. In these formulas, $S(\lambda_0)$ is the solar spectral irradiance for AM1.5 [28], and the spectral range of interest was considered with $\lambda_{\min} = 400$ nm and $\lambda_{\max} = 1100$ nm. The SSI absorption efficiency served as the cost function for optimization, for which the parameters $L, \zeta \in (0, 1), L_g, d_T, d_a,$ and θ were kept variable. The imaginary part of the relative permittivity of a-Si_{1-u}Ge_u:H with bandgap $E_g = 1.4$ eV is negligibly small for $\lambda_0 > 886$ nm, but the consequent lack of significant absorption for $\lambda_0 > 886$ nm can be ignored in a first study because the peak of AM1.5 solar irradiance spectrum is around 550 nm.

The grating geometries selected for numerical results can be fabricated experimentally. Sinusoidal grating templates can be fabricated by interference photolithography on photoresist [29]. Rectangular and trapezoidal gratings can be fabricated by conventional optical lithography followed by reactive ion etching or wet etching on single-crystal silicon wafers. Rectangular gratings can be defined with anisotropic silicon etchants such as Cl₂ or SF₆ on a 100-oriented crystalline-silicon wafers [30]. Trapezoidal gratings with variable taper angles can be fabricated by controlling the volumetric ratio of SF₆/O₂ and

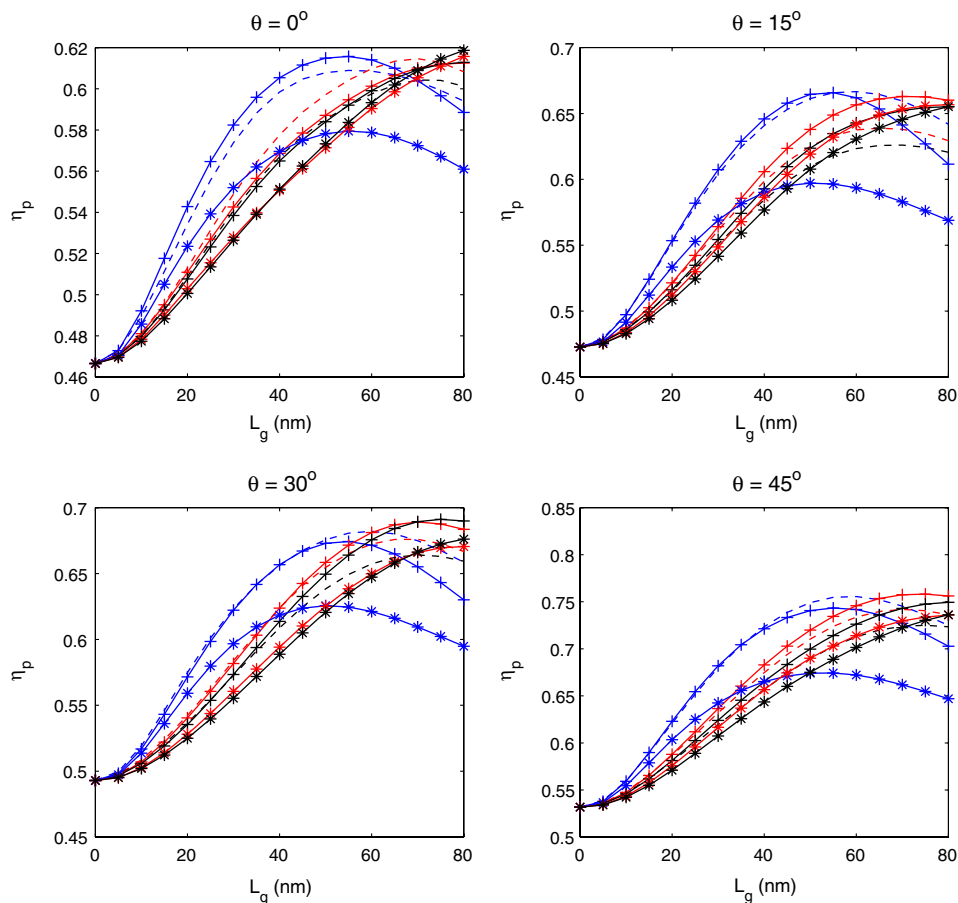


Fig. 5. (Color online) η_p versus L_g for $L = 400$ nm and $\theta \in \{0^\circ, 15^\circ, 30^\circ, 45^\circ\}$ for rectangular (blue curves), sinusoidal (red curves), and trapezoidal (black curves) corrugations. The duty cycle $\zeta = 0.3$ (dashed curves), 0.5 (curves with crosses), and 0.7 (curves with asterisks). The computations were made for a solar cell without ITO and AZO layers: $d_T = 0, d_a = L_g,$ and $\epsilon_a = \epsilon_{1n}$.

pressure during reactive ion etching of 100-oriented crystalline-silicon wafers [31]. Once the pattern is defined in the silicon or polymer grating master, metals such as aluminum can be sputtered over the template, thereby yielding a patterned metal surface with the desired nanoscale morphology [32].

Let us now discuss the numerical results for direct insolation (when the light is incident on the solar cell at a given angle of incidence) and diffuse insolation (when the light is incident from a wide range of directions with equal intensity). The results in Sections 4.A and 4.B hold for a solar cell without an ITO layer and an AZO layer: $d_T = 0$, $d_a = L_g$, and $\epsilon_a = \epsilon_{1n}$. The effects of the ITO and AZO layers are considered in Section 4.C.

A. Direct Insolation

1. Optimization with Fixed Period L

Let us begin with a surface-relief grating whose period $L = 400$ nm is fixed, but ζ , L_g , θ , and the corrugation-shape function $g(x)$ are variable. The three SSI absorption efficiencies η_p , η_s , and η are plotted against the corrugation height L_g in Figs. 5–7, respectively, for the angle of incidence $\theta \in \{0^\circ, 15^\circ, 30^\circ, 45^\circ\}$ and the duty cycle $\zeta \in \{0.3, 0.5, 0.7\}$.

A general feature of all the plots presented in these figures is that the SSI absorption efficiency is higher

for $L_g \neq 0$ than for $L_g = 0$, regardless of the angle of incidence and the polarization state of the incident light. In other words, a periodically corrugated back reflector yields a greater SSI absorption efficiency than one with a planar face, which is in accord with very early studies [5,6].

For p -polarized incident light, Fig. 5 shows that the maximum value of η_p is a function of L_g , ζ , and θ , and it also depends on the shape of the corrugation. For each of the four values of θ , Table 1 presents the combination of the corrugation shape, ζ , and L_g that maximizes η_p . The maximum achievable η_p is an increasing function of θ , while the optimal duty cycle is 0.5 or smaller and the optimal value of the corrugation height lies between 55 and 75 nm.

For s -polarized incident light and for a specific value of θ , the maximum value of η_s depends not only on ζ and L_g but also on the shape of the corrugation. The combination of the corrugation shape, ζ , and L_g that maximizes η_s for any one of the four different angles of incidence selected can be gleaned from Table 2. The optimal duty cycle lies between 0.3 and 0.7, while the optimal corrugation height is about 80 nm. Moreover, the maximum achievable η_s is not a strong function of θ . A comparison of Tables 1 and 2 shows that (i) the SSI absorption efficiency for s -polarized light is significantly smaller than that of p -polarized light and (ii) both the duty cycle and the

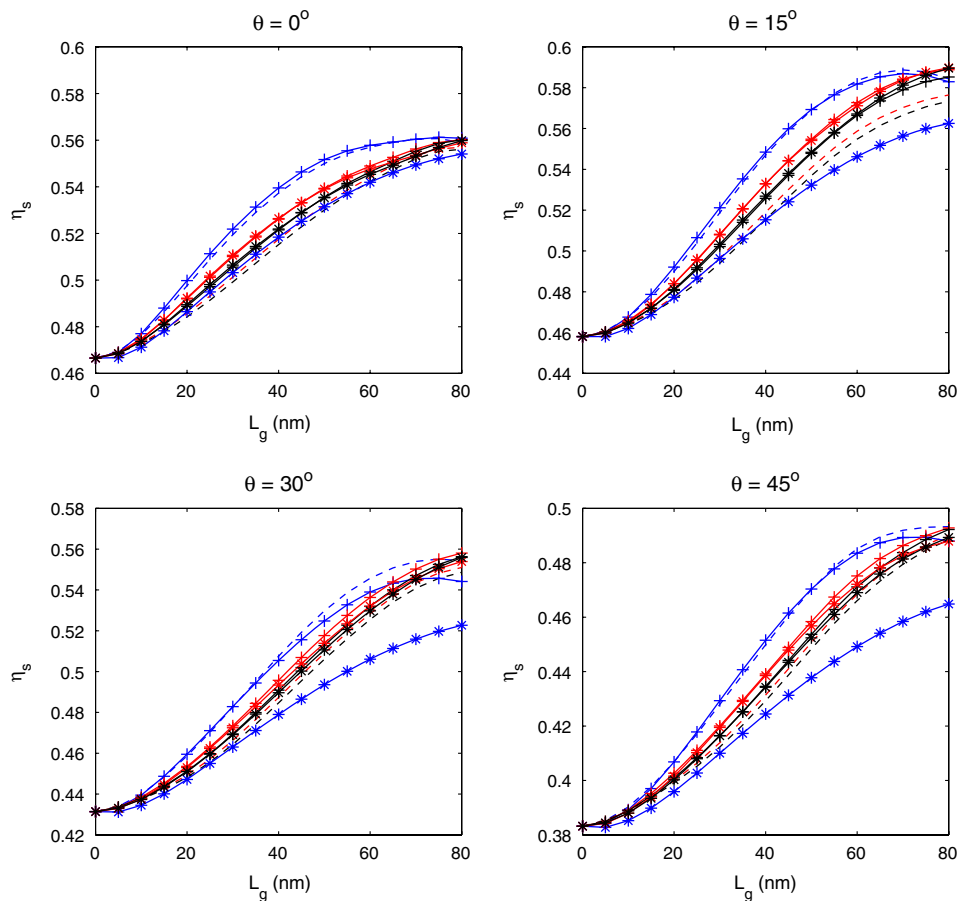


Fig. 6. (Color online) Same as Fig. 5 except that η_s is plotted instead of η_p .

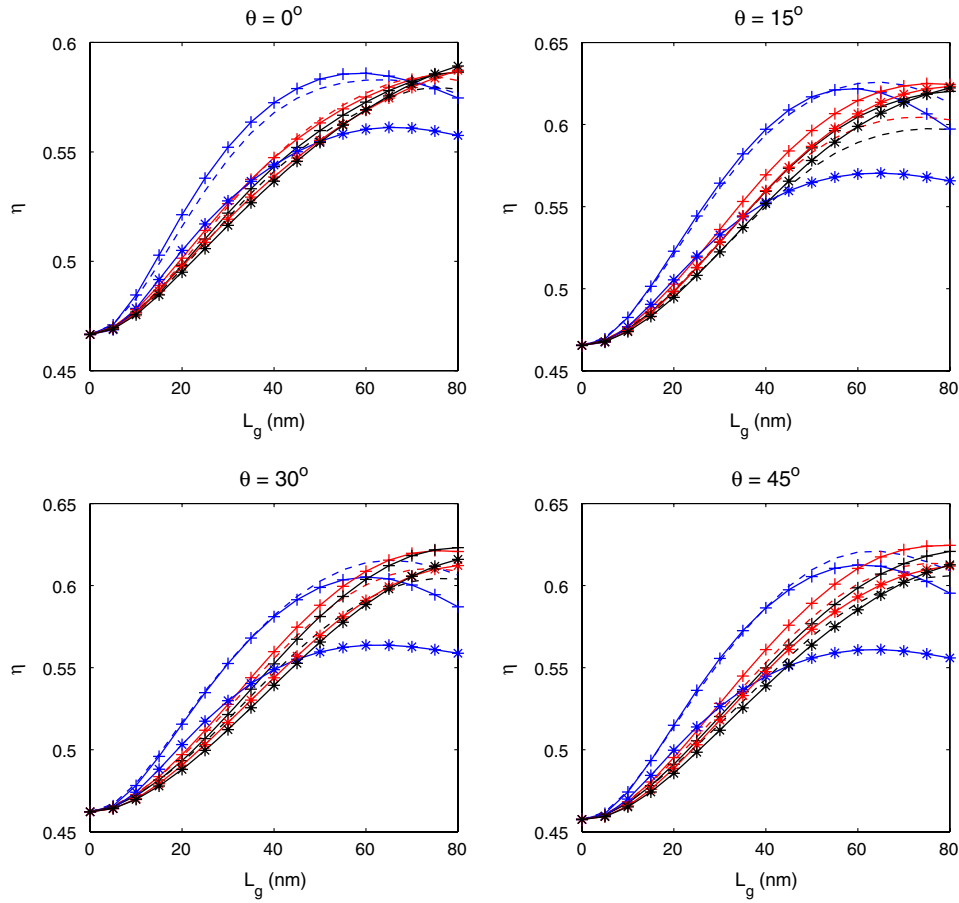


Fig. 7. (Color online) Same as Fig. 5, except that η is plotted instead of η_p .

corrugation height need to be larger for maximizing η_s than for maximizing η_p .

For unpolarized incident light, the maximum value of η and the values of ζ and L_g along with the shape of the corrugation that maximize η for

$\theta \in \{0^\circ, 15^\circ, 30^\circ, 45^\circ\}$ are presented in Table 3, having been obtained from the parametric plots presented in Fig. 7. The table shows that the maximum η is quite a weak function of the angle of incidence; however, corrugations of different shapes and/or duty cycle are required to maximize η .

The foregoing optimization was done simply by examining the parametric plots in Figs. 5–7. For better determination of the optimal parameters, we implemented the DEA explained in Section 3. The data provided in Tables 1–3 were used to define the search space and the initial guesses for the free parameters. The DEA was implemented—with 100 iterations and initial guess $\{\theta = 30^\circ, \zeta = 0.5, L_g = 70 \text{ nm}\}$ —separately for rectangular, sinusoidal, and trapezoidal corrugations.

The parameters θ^{opt} , ζ^{opt} , and L_g^{opt} that maximize the cost function η are presented in Table 4 for

Table 1. Corrugation Shape and Values of the Duty Cycle ζ and the Corrugation Height L_g that Maximize η_p for Four Values of θ , When $L = 400 \text{ nm}^a$

θ	Corrugation	ζ	L_g (nm)	η_p
0°	Rectangular	0.5	55	0.6157
15°	Rectangular	0.3	60	0.6666
30°	Trapezoidal	0.5	75	0.6911
45°	Sinusoidal	0.5	75	0.7581

^aThe results were obtained by inspection of the parametric plots in Fig. 5.

Table 2. Same as Table 1 Except That η_s Is Maximized and the Results Were Obtained by Inspection of the Parametric Plots in Fig. 6

θ	Corrugation	ζ	L_g (nm)	η_s
0°	Rectangular	0.5	75	0.5612
15°	Sinusoidal	0.7	80	0.5898
30°	Sinusoidal	0.5	80	0.5580
45°	Rectangular	0.3	80	0.4932

Table 3. Same as Table 1 Except That η Is Maximized and the Results Were Obtained by Inspection of the Parametric Plots in Fig. 7

θ	Corrugation	ζ	L_g (nm)	η
0°	Trapezoidal	0.7	80	0.5892
15°	Rectangular	0.7	65	0.6259
30°	Trapezoidal	0.5	80	0.6231
45°	Sinusoidal	0.5	80	0.6245

Table 4. Optimal Parameters $\{\theta^{\text{opt}}, \zeta^{\text{opt}}, L_g^{\text{opt}}\}$ to Maximize the SSI Absorption Efficiency η Delivered by the DEA for a Solar Cell Without ITO and AZO Layers: $d_T = 0$, $d_a = L_g$, and $\epsilon_a = \epsilon_{1n}$ ^a

Corrugation	θ^{opt}	ζ^{opt}	L_g^{opt} (nm)	η^{max}
Rectangular	14.52°	0.37	66.88	0.61
Sinusoidal	39.28°	0.5	80.00	0.62
Trapezoidal	39.69°	0.37	70.30	0.62

^aAll computations were made for $L = 400$ nm.

rectangular, sinusoidal, and trapezoidal corrugations. Remarkably, the same maximum SSI absorption efficiencies can be obtained, regardless of the choice of the corrugation-shape function. Thus, the exact shape of the corrugation does not matter—most likely because the corrugations are shallow in comparison to the free-space wavelength. The results for p - and s -polarized incidence conditions (not presented) showed that the optimal angles of incidence are strongly correlated with the maximum SSI absorption efficiencies and the polarization state, but not with shape of the corrugation. A duty cycle of around 0.38 and a corrugation height of about 70 nm are recommended for rectangular corrugations. The optimal duty cycle for the sinusoidal corrugation is polarization-dependent, but the optimal corrugation height of 80 nm is not. Both the optimal duty cycle and the corrugation height are polarization-dependent, when the corrugation is trapezoidal.

2. Optimization of the Period L

Next, we fixed the duty cycle ζ and the corrugation height L_g equal to the optimal values found in Section 4.A.1 (Table 4), and varied the period L and the angle of incidence θ . The incident light was taken to be unpolarized.

The SSI absorption efficiency η is presented as a function of L and θ in Fig. 8 for rectangular, sinusoidal, and trapezoidal corrugations. A comparison of the three panels in Fig. 8 indicates that the qualitative variation of η with L and θ does not depend strongly on the shape of the corrugation. The figure shows that higher SSI absorption efficiencies are obtained for a period between 400 and 600 nm for near-normal incidence of unpolarized light. For more oblique incidence, higher absorption efficiencies are obtained for L between 350 and 450 nm. The exact values of L and θ that maximize η are provided in Table 5.

The SSI absorption efficiency η as a function of L and θ for an unpolarized incident plane wave is presented in Fig. 9 when the back reflector is planar ($L_g = 0$ and $L_m = 30$ nm) and without a back reflector ($L_g = L_m = 0$). A comparison of Figs. 8 and 9 shows that η is greater with a periodically corrugated back reflector than either with a planar back reflector or without a back reflector at all.

B. Diffuse Insolation

Let us now suppose that the light is incident on the tandem solar cell for $\theta \in [0^\circ, 60^\circ]$, when the energy

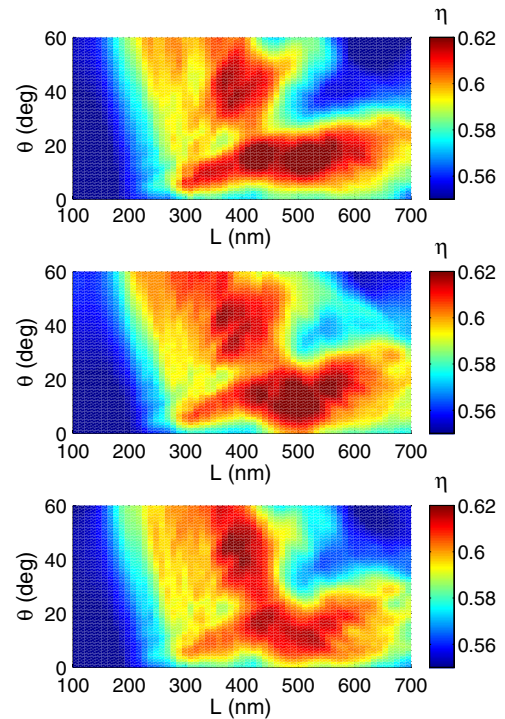


Fig. 8. (Color online) Variations of η with L and θ , the incident light being unpolarized. Top: $\zeta = 0.37$ and $L_g = 66.88$ nm for the rectangular corrugation. Center: $\zeta = 0.5$ and $L_g = 80$ nm for the sinusoidal corrugation. Bottom: $\zeta = 0.37$ and $L_g = 70.3$ nm for the trapezoidal corrugation. The computations were made for a solar cell without ITO and AZO layers: $d_T = 0$, $d_a = L_g$, and $\epsilon_a = \epsilon_{1n}$.

density of the incident light does not depend on the angle of incidence. This situation can also be considered as an equivalent of integration over time during the day for a solar cell that is fixed and not tracking the Sun. Now, to find the optimal parameters of the surface-relief grating, we computed the angularly averaged SSI absorption efficiency

$$\bar{\eta}(L, \zeta, L_g) = \frac{3}{\pi} \int_0^{\pi/3} \eta(L, \zeta, L_g, \theta) \cos \theta d\theta \quad (22)$$

for unpolarized incidence. The optimal grating parameters were found by inspection of the plots of angularly averaged efficiency versus the grating parameters ζ , L_g , and L .

Plots of $\bar{\eta}$ versus L_g are provided in Fig. 10 for corrugations of the chosen three shapes and

Table 5. Maximum Values of the SSI absorption Efficiency η and Optimal Parameters for Incident Unpolarized Light Obtained by Inspection of the Parametric Plots in Fig. 8^a

Corrugation	θ	L (nm)	η
Rectangular	15.25°	527	0.6287
Sinusoidal	11.19°	497	0.6250
Trapezoidal	45.76°	375	0.6211

^aThe duty cycle ζ and the corrugation height L_g were fixed at the optimal values obtained with fixed period $L = 400$ nm.

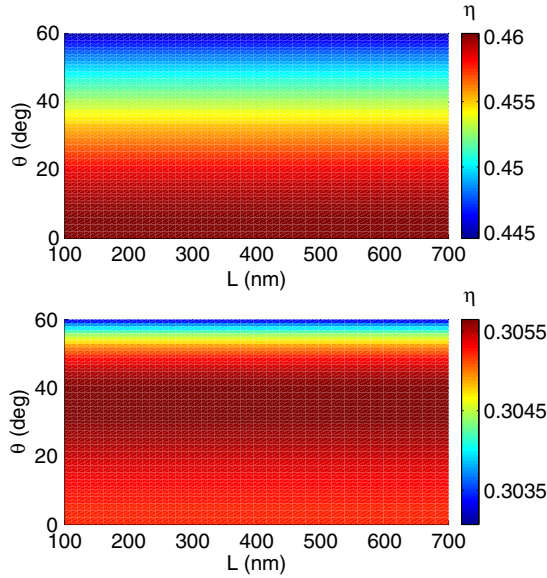


Fig. 9. (Color online) Same as Fig. 8 except that (top) $L_g = 0$ and $L_m = 30$ nm, and (bottom) $L_g = L_m = 0$.

$\zeta \in \{0.3, 0.5, 0.7\}$. The figure shows that, for unpolarized incident light, the grating with sinusoidal corrugations with $\zeta = 0.5$ and $L_g = 80$ nm should be chosen to maximize $\bar{\eta}$. All that now remains is to determine the value of L that maximizes $\bar{\eta}$ when $\zeta = 0.5$ and $L_g = 80$ nm. Inspection of the plots of $\bar{\eta}$ against L in Fig. 11 for the three types of corrugations lets us conclude that the optimal value of L and the maximum value of $\bar{\eta}$ are virtually independent of the shape of the corrugation. Thus, the combination $\{\zeta = 0.5, L_g = 80$ nm, $L = 433$ nm $\}$ maximizes $\bar{\eta}$ at ~ 0.5 , independently of the shape of the corrugation.

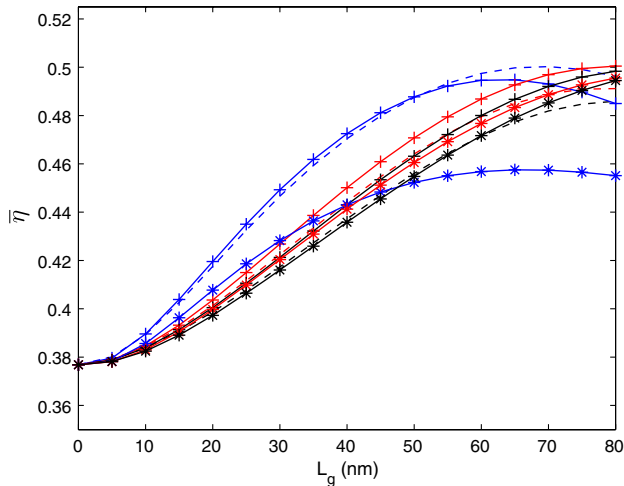


Fig. 10. (Color online) $\bar{\eta}$ versus L_g for $L = 400$ nm for rectangular (blue curves), sinusoidal (red curves), and trapezoidal (black curves) corrugations. The duty cycle $\zeta = 0.3$ (dashed curves), 0.5 (curves with crosses), and 0.7 (curves with asterisks). The grating with sinusoidal corrugations with $\zeta = 0.5$ and $L_g = 80$ nm maximizes $\bar{\eta}$ (at 0.5005). The computations were made for a solar cell without ITO and AZO layers: $d_T = 0$, $d_a = L_g$, and $\epsilon_a = \epsilon_{1n}$.

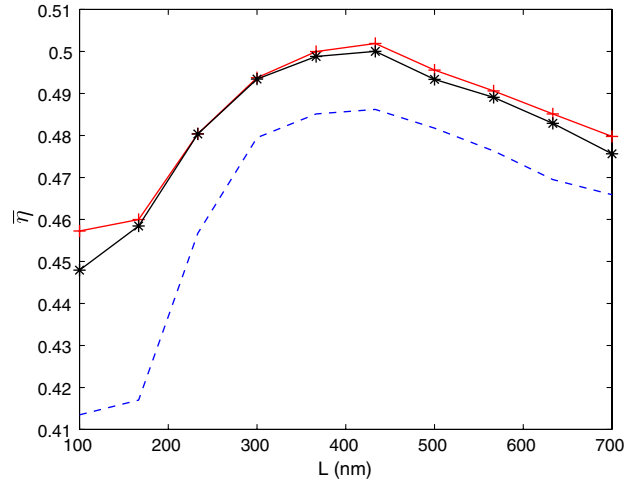


Fig. 11. (Color online) $\bar{\eta}$ versus L for a surface-relief grating with rectangular (blue dashed curve), sinusoidal (red crossed curve), or trapezoidal (black asterisk curve) corrugations, when $\zeta = 0.5$ and $L_g = 80$ nm. The computations were made for a solar cell without ITO and AZO layers: $d_T = 0$, $d_a = L_g$, and $\epsilon_a = \epsilon_{1n}$.

The grating parameters to maximize $\bar{\eta}$, as delivered by inspection of data computed using the RCWA algorithm, provided the initial guess to implement the DEA. The initial guess chosen was $\{\zeta = 0.5, L_g = 70$ nm, $L = 400$ nm $\}$. As many as 30 iterations were used for the DEA optimization. The optimal values of ζ , L_g , and L for each of the chosen shapes of the corrugations are presented in Table 6. Clearly, the maximum value of $\bar{\eta} \simeq 0.5$ for all three shapes. The optimal values ζ^{opt} , L_g^{opt} , and L^{opt} for the rectangular corrugation are smaller than their counterparts for the sinusoidal and the trapezoidal corrugations, but the differences are not very large.

A comparison of the results presented in Table 6 for diffuse insolation with those presented in Section 4.A.2 for direct insolation reveals that (i) the maximum SSI absorption efficiency for direct insolation ($\eta \simeq 0.62$) is higher than for diffuse insolation ($\bar{\eta} \simeq 0.5$) and (ii) the optimal period L^{opt} is generally higher for direct than diffuse insolation.

To delineate the contributions of the three intrinsic-semiconductor layers to the total absorbance, we computed the linear density of the rate of absorption

$$\frac{dQ(z)}{dz} = \frac{\omega\epsilon_0}{2} \text{Im}\{\epsilon_d(z)\} |E(z)|^2, \quad (23)$$

Table 6. Optimal Values $\{\zeta^{\text{opt}}, L_g^{\text{opt}}, L^{\text{opt}}\}$ of the Different Corrugation Shapes that Maximize η for Unpolarized Incident Light*

Corrugation	ζ^{opt}	L_g^{opt} (nm)	L^{opt} (nm)	$\bar{\eta}^{\text{max}}$
Rectangular	0.34	65	385	0.504
Sinusoidal	0.47	78	442	0.503
Trapezoidal	0.43	73	424	0.503

*The data were obtained using the DEA for a solar cell without ITO and AZO layers: $d_T = 0$, $d_a = L_g$, and $\epsilon_a = \epsilon_{1n}$.

and normalized it by the z -directed component

$$P_z^{\text{inc}} = \frac{1}{2} \sqrt{\frac{\epsilon_0}{\mu_0}} [|a_p^{(0)}|^2 + |a_s^{(0)}|^2] \cos \theta \quad (24)$$

of the time-averaged Poynting vector of the incident plane wave to get the ratio

$$\alpha(z) = \frac{dQ(z)/dz}{P_z^{\text{inc}}} = \frac{k_0 \text{Im}\{\epsilon_d(z)\} |E(z)|^2}{[|a_p^{(0)}|^2 + |a_s^{(0)}|^2] \cos \theta}. \quad (25)$$

As the integral of $\alpha(z)$ over $z \in [0, L_t]$ is the absorptance, $\alpha(z)$ may be called the absorptance density. This quantity was integrated over $\theta \in [0, \pi/3]$ for an unpolarized plane wave to obtain the angularly averaged local absorptance density

$$\bar{\alpha}(L, \zeta, L_g, \lambda_0, z) = \frac{3}{\pi} \int_0^{\pi/3} [\alpha(L, \zeta, L_g, \theta, \lambda_0, z) |_{a_p^{(0)}=a_s^{(0)}}] \times \cos \theta d\theta. \quad (26)$$

Plots of $\bar{\alpha}(L, \zeta, L_g, \lambda_0, z)$ are provided in Fig. 12, for a rectangular surface-relief grating with optimal grating parameters delivered by DEA (Table 6): $\zeta = 0.34$, $L_g = 65$ nm, and $L = 385$ nm. When $\lambda_0 < 500$ nm, most of the absorption takes place in the $3i$ layer ($E_g = 1.69$ eV); when $500 \text{ nm} < \lambda_0 < 600$ nm, both the $3i$ and the $2i$ ($E_g = 1.6$ eV) layers absorb more than the $1i$ layer ($E_g = 1.4$ eV); when

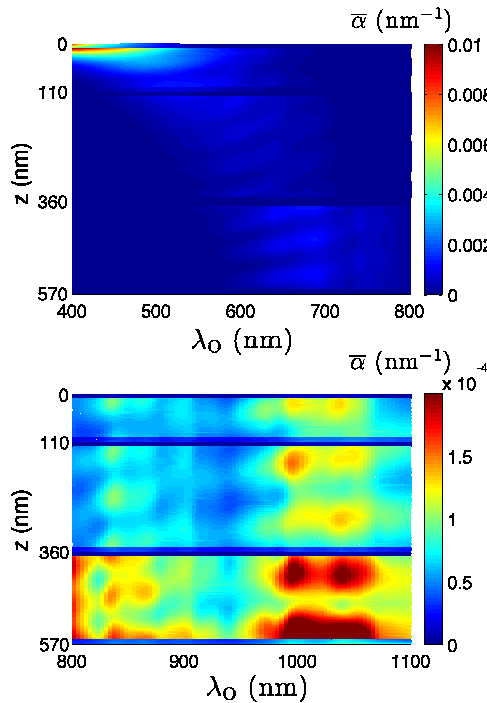


Fig. 12. (Color online) Angularly averaged local absorptance density $\bar{\alpha}$ versus λ_0 and z for unpolarized incident light in the region $0 < z < L_d$ for a solar cell without an ITO or an AZO layer when the optimum surface-relief grating was used as the backing metallic layer: $\zeta = 0.34$, $L_g = 65$ nm, $L = 385$ nm, $d_T = 0$, $d_a = L_g$, $\epsilon_a = \epsilon_{1n}$, and the corrugations are rectangular.

$600 \text{ nm} < \lambda_0 < 700$ nm, absorption is higher in the $2i$ and $1i$ layers than in the $3i$ layer; when $\lambda_0 > 700$ nm, most of the light is being absorbed by the $3i$ layer. The figure clearly shows the benefit of using a tandem solar cell as opposed to a single-junction cell because different intrinsic-semiconductor layers can absorb light in different spectral regimes, thereby enhancing the overall light absorption. The local absorptance density is very low when $\lambda_0 > 800$ nm, as should be expected due to the negligible imaginary parts of the relative permittivities of the semiconductor materials in this spectral regime.

C. Effect of ITO and AZO Layers on the Optimal Grating Profile

Let us now examine the results for a tandem solar cell with an ITO layer at the top and an AZO layer between the metal and the $1n$ layer. For ITO, we used experimentally obtained values of the complex refractive indexes at an air/ITO interface [33, Fig 3]. For AZO, the refractive indexes were obtained by using a single-oscillator model developed for AZO films deposited by reactive magnetron sputtering at a substrate temperature of 170°C [34]. The thickness of the ITO layer was fixed at $d_T = 200$ nm, whereas the thickness of the AZO layer was kept variable: $d_a = L_g + 10$ nm. For the limited purpose of delineating the overall effect of the ITO and AZO layers on the solar cell, only diffuse insolation was considered.

The plots of $\bar{\eta}$ versus L_g for the three types of surface-relief gratings with different values of ζ are presented in Fig. 13. A comparison of Figs. 13 and 10 shows that $\bar{\eta}$ is generally higher when an ITO layer is present—which is reasonable because of the additional absorption by the ITO layer. Inspection of Fig. 13 shows that $\bar{\eta}$ is maximum (≈ 0.6104) when $\zeta = 0.3$, $L_g = 150$ nm, and the corrugations are rectangular. The plot of $\bar{\eta}$ versus L in Fig. 14 for the three types of surface-relief gratings with $\zeta = 0.3$

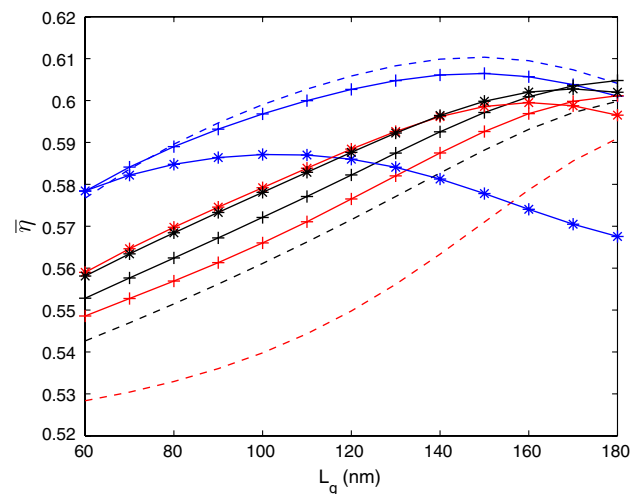


Fig. 13. (Color online) Same as Fig. 10 except that the ITO and AZO layers are also present: $d_T = 200$ nm and $d_a = L_g + 10$ nm.

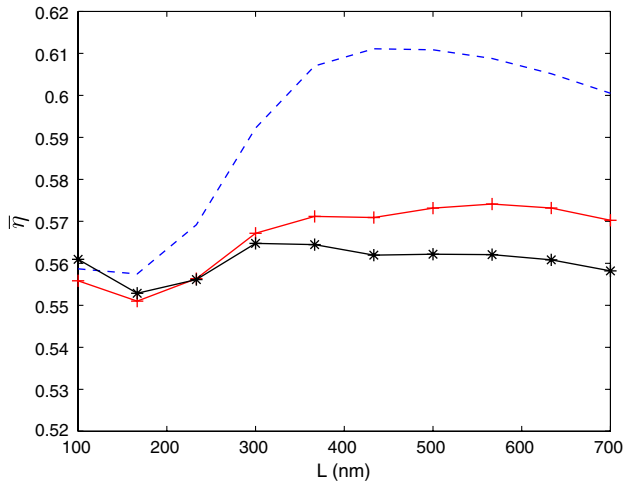


Fig. 14. (Color online) Same as Fig. 11 except that the ITO and AZO layers are also present: $d_T = 200$ nm, $\zeta = 0.3$, $L_g = 150$ nm, and $d_a = L_g + 10$ nm.

and $L_g = 150$ nm shows that $\bar{\eta}$ is maximum when the corrugations are rectangular and $L \approx 433$ nm.

A comparison of the optimal value of L obtained by inspection for the solar cell with the ITO and AZO layers with those values presented in Table 6 indicates that the optimal period of the grating does not vary significantly with the addition of ITO and AZO layers.

Finally, to see the effect of ITO and AZO layers on the local absorptance density in the solar cell, $\bar{\alpha}(L, \zeta, L_g, \lambda_0, z)$ is presented in Fig. 15 versus λ_0 and z in the region $0 < z < L_d$ when $L = 433$ nm, $d_T = 200$ nm, $\zeta = 0.3$, $L_g = 150$ nm, and $d_a = L_g + 10$ nm. In the semiconductor region

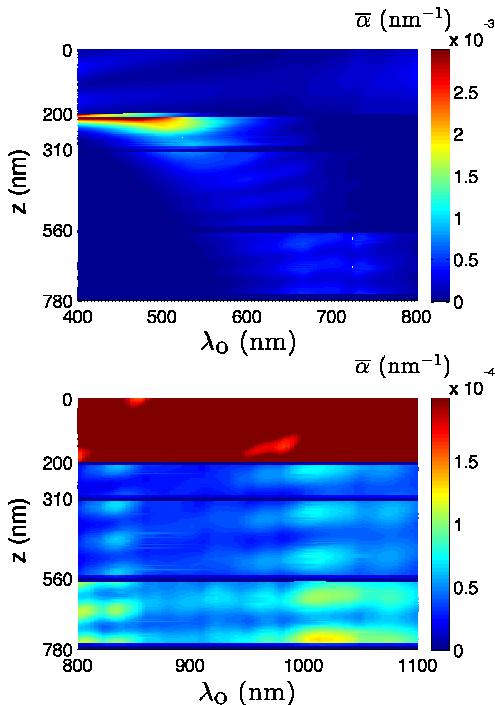


Fig. 15. (Color online) Same as Fig. 12 except that $L = 433$ nm, $d_T = 200$ nm, $\zeta = 0.3$, $L_g = 150$ nm, and $d_a = L_g + 10$ nm.

($d_T < z < L_d - 10$ nm), the variation of $\bar{\alpha}$ with z is similar to that when the ITO and AZO layers are absent (Fig. 12); however, $\bar{\alpha}$ is generally lower in magnitude. In the ITO layer, $\bar{\alpha}$ is lower than in the semiconductor region when $400 \text{ nm} < \lambda_0 < 750 \text{ nm}$. When $750 \text{ nm} < \lambda_0 < 1100 \text{ nm}$, most of the absorption takes place in the ITO layer. Absorption in the AZO layer is absent in the 400–1100 nm wavelength range [34].

5. Conclusion

The optimal values of the duty cycle ζ , the corrugation height L_g , and the period L of an aluminum surface-relief grating with corrugations of various shapes were obtained from direct and indirect insolation for a thin-film tandem solar cell made of hydrogenated-amorphous silicon alloys. The thicknesses and the compositions of the various semiconductor layers had been fixed from electrical considerations. The SSI absorption efficiency of the tandem solar cell was optimized for an AM1.5 solar irradiance spectrum and the wavelength range considered was 400–1100 nm. Optimization for direct insolation was done first by inspection of the dependences of the SSI absorption efficiency on the grating parameters and the angle of incidence, followed by the implementation of an evolutionary algorithm. For diffuse insolation, the same procedure was repeated except that the SSI absorption efficiency was averaged over the angle of incidence. Furthermore, the effect of the inclusion of an ITO layer at the front and an AZO layer between the semiconductor and the metallic back reflector was also studied.

For direct insolation, when the period $L = 400$ nm is fixed, we found that (i) the maximum SSI absorption efficiency is significantly smaller for s - than p -polarized incident light, (ii) ζ and L_g need to be larger for s - than p -polarized incident light to maximize SSI absorption efficiency, and (iii) the same maximum value of SSI absorption efficiency can be achieved—regardless of the shape of the corrugation in each unit cell of the metallic back reflector when the ITO and AZO layers are absent. However, when the period is allowed to be different for different directions of incoming light, the optimal period (i) $L^{\text{opt}} \in (350, 450)$ nm when the incidence angle is large and (ii) $L^{\text{opt}} \in (400, 600)$ nm when the incidence is near normal—again, regardless of the shape of the corrugation. For diffuse insolation with equal intensity for $\theta \in [0^\circ, 60^\circ]$, the angularly averaged SSI absorption efficiency can also be maximized for any choice of the corrugation-shape function. However, the maximum efficiency for diffuse insolation is about 20% smaller than for direct insolation.

The inclusion of an ITO layer at the front and the insertion of an AZO layer between the semiconductor and the metallic back reflector decrease the absorption in the semiconductor layers. With the ITO and AZO layers present, the maximum SSI absorption efficiency was achieved with a periodic corrugation of rectangular shape and a depth ($L_g = 150$ nm) that

was twice the optimal depth obtained without the ITO and AZO layers. However, the optimal period of the periodic corrugation did not critically depend on the presence of the ITO and AZO layers.

Let us note that the enhancement in the SSI absorption efficiency when a metallic surface-relief grating is used as the back reflector is due to the capability of the grating to guide SPP waves and waveguide modes [4–6,11,35]. An SPP wave is guided by the grating when the wavenumber of a Floquet harmonic and the wavenumber of the possible SPP wave match each other. The possibility of this match can be further increased by the use of a compound surface-relief grating [36,37]. We conclude this paper with the hope that our optimization study will assist in the selection of surface-relief-grating profiles that enhance the efficiencies of tandem solar cells exploiting hydrogenated-amorphous silicon alloys.

We thank an anonymous reviewer for several constructive suggestions. Partial support for this work was provided by the U.S. National Science Foundation via Grant No. DMR-1125591 and some computations were performed on a computer purchased via NSF Grant No. CNS-0958512. AL acknowledges ongoing support of his research by the Charles Godfrey Binder Endowment at Penn State.

References

1. A. Gombert and A. Luque, "Photonics in photovoltaic systems," *Phys. Status Solidi A* **205**, 2757–2765 (2008).
2. D. M. Schaadt, B. Feng, and E. T. Yu, "Enhanced semiconductor optical absorption via surface plasmon excitation in metal nanoparticles," *Appl. Phys. Lett.* **86**, 063106 (2005).
3. V. E. Ferry, L. A. Sweatlock, D. Pacifici, and H. A. Atwater, "Plasmonic nanostructure design for efficient light coupling into solar cells," *Nano Lett.* **8**, 4391–4397 (2008).
4. M. A. Green and S. Pillai, "Harnessing plasmonics for solar cells," *Nat. Photonics* **6**, 130–132 (2012).
5. P. Sheng, A. N. Bloch, and R. S. Stepleman, "Wavelength-selective absorption enhancement in thin-film solar cells," *Appl. Phys. Lett.* **43**, 579–581 (1983).
6. C. Heine and R. H. Morf, "Submicrometer gratings for solar energy applications," *Appl. Opt.* **34**, 2476–2482 (1995).
7. R. Singh, "Why silicon is and will remain the dominant photovoltaic material," *J. Nanophoton.* **3**, 032503 (2009).
8. S. J. Fonash, *Solar Cell Device Physics*, 2nd ed. (Academic, 2010), pp. 68–102.
9. F.-J. Haug, T. Söderström, O. Cubero, V. Terrazzoni-Daudrix, and C. Ballif, "Plasmonic absorption in textured silver back reflectors of thin film solar cells," *J. Appl. Phys.* **104**, 064509 (2008).
10. J. Chen, Q. Wang, and H. Li, "Microstructured design of metallic diffraction gratings for light trapping in thin-film silicon solar cells," *Opt. Commun.* **283**, 5236–5244 (2010).
11. S. Xiao, E. Stassen, and N. A. Mortensen, "Ultrathin silicon solar cells with enhanced photocurrents assisted by plasmonic nanostructures," *J. Nanophoton.* **6**, 061503 (2012).
12. A. Naqavi, K. Söderström, F.-J. Haug, V. Paeder, T. Scharf, H. P. Herzig, and C. Ballif, "Enhanced light trapping in realistic thin film solar cells using one-dimensional gratings," *Proc. SPIE* **8065**, 80650A (2011).
13. A. Čampa, O. Isabella, R. van Erven, P. Peeters, H. Borg, J. Krč, M. Topič, and M. Zeman, "Optimal design of periodic surface texture for thin-film a-Si:H solar cells," *Prog. Photovoltaics* **18**, 160–167 (2010).
14. M. G. Moharam and T. K. Gaylord, "Diffraction analysis of dielectric surface-relief gratings," *J. Opt. Soc. Am.* **72**, 1385–1392 (1982).
15. N. Chateau and J.-P. Hugonin, "Algorithm for the rigorous coupled-wave analysis of grating diffraction," *J. Opt. Soc. Am. A* **11**, 1321–1331 (1994).
16. M. Agrawal and M. Frei, "Rigorous optical modeling and optimization of thin-film photovoltaic cells with textured transparent conductive oxides," *Prog. Photovolt.* **20**, 442–451 (2012).
17. M. Agrawal, M. Frei, Y. Bhatnagar, T. Repmann, K. Witting, J. Schroeder, and C. Eberspacher, "Comprehensive experimental and numerical optimization of surface morphology of transparent conductive oxide films for tandem thin film photovoltaic cells," in *Proc. 35th IEEE Photovoltaic Specialists Conference (PVSC)* (IEEE, 2010).
18. R. Storn and K. Price, "Differential evolution—a simple and efficient heuristic for global optimization over continuous spaces," *J. Global Optim.* **11**, 341–359 (1997).
19. K. Price, R. Storn, and J. Lampinen, *Differential Evolution: A Practical Approach to Global Optimization* (Springer, 2005).
20. T. Tušar and B. Filipič, "Differential evolution versus genetic algorithms in multiobjective optimization," in *Evolutionary Multi-Criterion Optimization*, S. Obayashi, K. Deb, C. Poloni, T. Hiroyasu, and T. Murata, eds. (Springer, 2007), pp. 257–271.
21. M. Faryad, A. S. Hall, G. D. Barber, T. E. Mallouk, and A. Lakhtakia, "Excitation of multiple surface-plasmon-polariton waves guided by the periodically corrugated interface of a metal and a periodic multilayered isotropic dielectric material," *J. Opt. Soc. Am. B* **29**, 704–713 (2012).
22. M. Faryad and A. Lakhtakia, "Grating-coupled excitation of multiple surface plasmon-polariton waves," *Phys. Rev. A* **84**, 033852 (2011).
23. M. G. Moharam, E. B. Grann, and D. A. Pommet, "Formulation for stable and efficient implementation of the rigorous coupled-wave analysis of binary gratings," *J. Opt. Soc. Am. A* **12**, 1068–1076 (1995).
24. We used the DEA code available at: <http://www1.icsi.berkeley.edu/storn/code.html>.
25. A. S. Ferlauto, G. M. Ferreira, J. M. Pearce, C. R. Wronski, R. W. Collins, X. Deng, and G. Ganguly, "Analytical model for the optical functions of amorphous semiconductors from the near-infrared to ultraviolet: applications in thin film photovoltaics," *J. Appl. Phys.* **92**, 2424–2436 (2002).
26. A. D. Rakić, "Algorithm for the determination of intrinsic optical constants of metal films: application to aluminum," *Appl. Opt.* **34**, 4755–4767 (1995).
27. B. B. Van Aken, C. Devilee, M. Dörenkämper, M. Geusebroek, M. Heijna, J. Löffler, and W. J. Soppe, "PECVD deposition of a-Si:H and μ -Si:H using a linear RF source," *Proc. SPIE* **6651**, 66510C (2007).
28. http://pvcfrom.pveducation.org/APPEND/Am1_5.htm (accessed 21 July 2012).
29. A. Shishido, I. Divilansky, G. L. Egan, I. C. Khoo, T. S. Mayer, S. Nishimura, G. L. Egan, and T. E. Mallouk, "Direct fabrication of two-dimensional titania arrays using interference photolithography," *Appl. Phys. Lett.* **79**, 3332–3334 (2001).
30. D. L. Flamm, "Mechanisms of silicon etching in fluorine- and chlorine-containing plasmas," *Pure Appl. Chem.* **62**, 1709–1720 (1990).
31. H. Jansen, M. Boer, R. Legtenberg, and M. J. Elwenspoek, "The black silicon method: a universal method for determining the parameter setting of a fluorine-based reactive ion etcher in deep silicon trench etching with profile control," *J. Micromech. Microeng.* **5**, 115–120 (1995).
32. P. Nagpal, N. C. Lindquist, S.-H. Oh, and D. J. Norris, "Ultra-smooth patterned metals for plasmonics and metamaterials," *Science* **325**, 594–597 (2009).
33. R. A. Synowicki, "Spectroscopic ellipsometry characterization of indium tin oxide film microstructure and optical constants," *Thin Solid Films* **313**, 394–397 (1998).

34. X.-Y. Gao, Y. Liang, and Q.-G. Lin, "Analysis of the optical constants of aluminum-doped zinc oxide films by using the single-oscillator model," *J. Korean Phys. Soc.* **57**, 710–714 (2010).
35. M. Faryad and A. Lakhtakia, "Enhanced absorption of light due to multiple surface-plasmon-polariton waves," *Proc. SPIE* **8110**, 81100F (2011).
36. I. Dolev, M. Volodarsky, G. Porat, and A. Arie, "Multiple coupling of surface plasmons in quasiperiodic gratings," *Opt. Lett.* **36**, 1584–1586 (2011).
37. M. Faryad and A. Lakhtakia, "Excitation of multiple surface-plasmon-polariton waves using a compound surface-relief grating," *J. Nanophoton.* **6**, 061701 (2012).